

3D Gaussian Splatting for Real-Time Radiance Field Rendering

BERNHARD KERBL*, Inria, Université Côte d’Azur, France

GEORGIOS KOPANAS*, Inria, Université Côte d’Azur, France

THOMAS LEIMKÜHLER, Max-Planck-Institut für Informatik, Germany

GEORGE DRETTAKIS, Inria, Université Côte d’Azur, France



Fig. 1. Our method achieves real-time rendering of radiance fields with quality that equals the previous method with the best quality [Barron et al. 2022], while only requiring optimization times competitive with the fastest previous methods [Fridovich-Keil and Yu et al. 2022; Müller et al. 2022]. Key to this performance is a novel 3D Gaussian scene representation coupled with a real-time differentiable renderer, which offers significant speedup to both scene optimization and novel view synthesis. Note that for comparable training times to InstantNGP [Müller et al. 2022], we achieve similar quality to theirs; while this is the maximum quality they reach, by training for 51min we achieve state-of-the-art quality, even slightly better than Mip-NeRF360 [Barron et al. 2022].

Radiance Field methods have recently revolutionized novel-view synthesis of scenes captured with multiple photos or videos. However, achieving high visual quality still requires neural networks that are costly to train and render, while recent faster methods inevitably trade off speed for quality. For unbounded and complete scenes (rather than isolated objects) and 1080p resolution rendering, no current method can achieve real-time display rates. We introduce three key elements that allow us to achieve state-of-the-art visual quality while maintaining competitive training times and importantly allow **high-quality real-time (≥ 30 fps) novel-view synthesis at 1080p resolution**. First, starting from sparse points produced during camera calibration, we represent the scene with 3D Gaussians that preserve desirable properties of continuous volumetric radiance fields for scene optimization while **avoiding unnecessary computation in empty space**; Second, we perform interleaved optimization/density control of the 3D Gaussians, notably optimizing anisotropic covariance to achieve an accurate representation of the scene; Third, we develop a fast visibility-aware rendering algorithm that supports **anisotropic splatting** and both accelerates training and allows real-time rendering. We demonstrate state-of-the-art visual quality and real-time rendering on several established datasets.

CCS Concepts: • Computing methodologies → Rendering; Point-based models; Rasterization; Machine learning approaches.

*Both authors contributed equally to the paper.

Authors’ addresses: Bernhard Kerbl, bernhard.kerbl@inria.fr, Inria, Université Côte d’Azur, France; Georgios Kopanas, georgios.kopanas@inria.fr, Inria, Université Côte d’Azur, France; Thomas Leimkühler, thomas.leimkuehler@mpi-inf.mpg.de, Max-Planck-Institut für Informatik, Germany; George Drettakis, george.drettakis@inria.fr, Inria, Université Côte d’Azur, France.

Publication rights licensed to ACM. ACM acknowledges that this contribution was authored or co-authored by an employee, contractor or affiliate of a national government. As such, the Government retains a nonexclusive, royalty-free right to publish or reproduce this article, or to allow others to do so, for Government purposes only.

© 2023 Copyright held by the owner/author(s). Publication rights licensed to ACM.

0730-0301/2023/8-ART1 \$15.00

<https://doi.org/10.1145/3592433>

Additional Key Words and Phrases: novel view synthesis, radiance fields, 3D gaussians, real-time rendering

ACM Reference Format:

Bernhard Kerbl, Georgios Kopanas, Thomas Leimkühler, and George Drettakis. 2023. 3D Gaussian Splatting for Real-Time Radiance Field Rendering. *ACM Trans. Graph.* 42, 4, Article 1 (August 2023), 14 pages. <https://doi.org/10.1145/3592433>

1 INTRODUCTION

Meshes and points are the most common 3D scene representations because they are explicit and are a good fit for fast GPU/CUDA-based rasterization. In contrast, recent Neural Radiance Field (NeRF) methods build on **continuous scene representations**, typically optimizing a Multi-Layer Perceptron (MLP) using volumetric **ray-marching** for novel-view synthesis of captured scenes. Similarly, the most efficient radiance field solutions to date build on continuous representations by interpolating values stored in, e.g., voxel [Fridovich-Keil and Yu et al. 2022] or hash [Müller et al. 2022] grids or points [Xu et al. 2022]. While the continuous nature of these methods helps optimization, the **stochastic sampling required for rendering is costly and can result in noise**. We introduce a new approach that combines the best of both worlds: our 3D Gaussian representation allows optimization with state-of-the-art (SOTA) visual quality and competitive training times, while our **tile-based splatting** solution ensures real-time rendering at SOTA quality for 1080p resolution on several previously published datasets [Barron et al. 2022; Hedman et al. 2018; Knapitsch et al. 2017] (see Fig. 1).

Our goal is to allow real-time rendering for scenes captured with multiple photos, and create the representations with optimization times as fast as the most efficient previous methods for typical real scenes. Recent methods achieve fast training [Fridovich-Keil

and Yu et al. 2022; Müller et al. 2022], but struggle to achieve the visual quality obtained by the current SOTA NeRF methods, i.e., Mip-NeRF360 [Barron et al. 2022], which requires up to 48 hours of training time. The fast – but lower-quality – radiance field methods can achieve interactive rendering times depending on the scene (10–15 frames per second), but fall short of real-time rendering at high resolution.

Our solution builds on three main components. We first introduce **3D Gaussians as a flexible and expressive scene representation**. We start with the same input as previous NeRF-like methods, i.e., cameras calibrated with Structure-from-Motion (SfM) [Snavely et al. 2006] and initialize the set of 3D Gaussians with the sparse point cloud produced for free as part of the SfM process. In contrast to most point-based solutions that require Multi-View Stereo (MVS) data [Aliev et al. 2020; Kopanas et al. 2021; Rückert et al. 2022], we achieve high-quality results with only SfM points as input. Note that for the NeRF-synthetic dataset, our method achieves high quality even with random initialization. We show that 3D Gaussians are an excellent choice, since they are a differentiable volumetric representation, but they can also be **rasterized very efficiently by projecting them to 2D, and applying standard α -blending**, using an equivalent image formation model as NeRF. The second component of our method is optimization of the properties of the **3D Gaussians – 3D position, opacity α , anisotropic covariance, and spherical harmonic (SH) coefficients – interleaved with adaptive density control steps, where we add and occasionally remove 3D Gaussians during optimization**. The optimization procedure produces a reasonably compact, unstructured, and precise representation of the scene (1–5 million Gaussians for all scenes tested). The third and final element of our method is our real-time rendering solution that uses fast GPU sorting algorithms and is inspired by tile-based rasterization, following recent work [Lassner and Zollhofer 2021]. However, thanks to our 3D Gaussian representation, we can perform anisotropic splatting that respects visibility ordering – thanks to sorting and α -blending – and enable a fast and accurate backward pass by tracking the traversal of as many sorted splats as required.

To summarize, we provide the following contributions:

- The introduction of anisotropic 3D Gaussians as a high-quality, unstructured representation of radiance fields.
- An optimization method of 3D Gaussian properties, interleaved with adaptive density control that creates high-quality representations for captured scenes.
- A fast, differentiable rendering approach for the GPU, which is visibility-aware, allows anisotropic splatting and fast back-propagation to achieve high-quality novel view synthesis.

Our results on previously published datasets show that we can optimize our 3D Gaussians from multi-view captures and achieve equal or better quality than the best quality previous implicit radiance field approaches. We also can achieve training speeds and quality similar to the fastest methods and importantly provide the first *real-time rendering* with high quality for novel-view synthesis.

2 RELATED WORK

We first briefly overview traditional reconstruction, then discuss point-based rendering and radiance field work, discussing their

similarity; radiance fields are a vast area, so we focus only on directly related work. For complete coverage of the field, please see the excellent recent surveys [Tewari et al. 2022; Xie et al. 2022].

2.1 Traditional Scene Reconstruction and Rendering

The first novel-view synthesis approaches were based on light fields, first densely sampled [Gortler et al. 1996; Levoy and Hanrahan 1996] then allowing unstructured capture [Buehler et al. 2001]. The advent of Structure-from-Motion (SfM) [Snavely et al. 2006] enabled an entire new domain where a collection of photos could be used to synthesize novel views. SfM estimates a sparse point cloud during camera calibration, that was initially used for simple visualization of 3D space. Subsequent multi-view stereo (MVS) produced impressive full 3D reconstruction algorithms over the years [Goesele et al. 2007], enabling the development of several view synthesis algorithms [Chaurasia et al. 2013; Eisemann et al. 2008; Hedman et al. 2018; Kopanas et al. 2021]. All these methods *re-project* and *blend* the input images into the novel view camera, and use the geometry to guide this re-projection. These methods produced excellent results in many cases, but typically cannot completely recover from unreconstructed regions, or from “over-reconstruction”, when MVS generates nonexistent geometry. Recent neural rendering algorithms [Tewari et al. 2022] vastly reduce such artifacts and avoid the overwhelming cost of storing all input images on the GPU, outperforming these methods on most fronts.

2.2 Neural Rendering and Radiance Fields

Deep learning techniques were adopted early for novel-view synthesis [Flynn et al. 2016; Zhou et al. 2016]; CNNs were used to estimate blending weights [Hedman et al. 2018], or for texture-space solutions [Riegler and Koltun 2020; Thies et al. 2019]. The use of MVS-based geometry is a major drawback of most of these methods; in addition, the use of CNNs for final rendering frequently results in temporal flickering.

Volumetric representations for novel-view synthesis were initiated by Soft3D [Penner and Zhang 2017]; deep-learning techniques coupled with volumetric ray-marching were subsequently proposed [Henzler et al. 2019; Sitzmann et al. 2019] building on a continuous differentiable density field to represent geometry. Rendering using volumetric ray-marching has a significant cost due to the large number of samples required to query the volume. Neural Radiance Fields (NeRFs) [Mildenhall et al. 2020] introduced importance sampling and positional encoding to improve quality, but used a large Multi-Layer Perceptron negatively affecting speed. The success of NeRF has resulted in an explosion of follow-up methods that address quality and speed, often by introducing regularization strategies; the current state-of-the-art in image quality for novel-view synthesis is Mip-NeRF360 [Barron et al. 2022]. While the rendering quality is outstanding, training and rendering times remain extremely high; we are able to equal or in some cases surpass this quality while providing fast training and real-time rendering.

The most recent methods have focused on faster training and/or rendering mostly by exploiting three design choices: the use of spatial data structures to store (neural) features that are subsequently interpolated during volumetric ray-marching, different encodings,

and MLP capacity. Such methods include different variants of space discretization [Chen et al. 2022b,a; Fridovich-Keil and Yu et al. 2022; Garbin et al. 2021; Hedman et al. 2021; Reiser et al. 2021; Takikawa et al. 2021; Wu et al. 2022; Yu et al. 2021], codebooks [Takikawa et al. 2022], and encodings such as hash tables [Müller et al. 2022], allowing the use of a smaller MLP or foregoing neural networks completely [Fridovich-Keil and Yu et al. 2022; Sun et al. 2022].

Most notable of these methods are InstantNGP [Müller et al. 2022] which uses a hash grid and an occupancy grid to accelerate computation and a smaller MLP to represent density and appearance; and Plenoxels [Fridovich-Keil and Yu et al. 2022] that use a sparse voxel grid to interpolate a continuous density field, and are able to forgo neural networks altogether. Both rely on Spherical Harmonics: the former to represent directional effects directly, the latter to encode its inputs to the color network. While both provide outstanding results, these methods can still struggle to represent empty space effectively, depending in part on the scene/capture type. In addition, image quality is limited in large part by the choice of the structured grids used for acceleration, and rendering speed is hindered by the need to query many samples for a given ray-marching step. The unstructured, explicit GPU-friendly 3D Gaussians we use achieve faster rendering speed and better quality without neural components.

2.3 Point-Based Rendering and Radiance Fields

Point-based methods efficiently render disconnected and unstructured geometry samples (i.e., point clouds) [Gross and Pfister 2011]. In its simplest form, point sample rendering [Grossman and Dally 1998] rasterizes an unstructured set of points with a fixed size, for which it may exploit natively supported point types of graphics APIs [Sainz and Pajarola 2004] or parallel software rasterization on the GPU [Laine and Karras 2011; Schütz et al. 2022]. While true to the underlying data, point sample rendering suffers from holes, causes aliasing, and is strictly discontinuous. Seminal work on high-quality point-based rendering addresses these issues by “splatting” point primitives with an extent larger than a pixel, e.g., circular or elliptic discs, ellipsoids, or surfels [Botsch et al. 2005; Pfister et al. 2000; Ren et al. 2002; Zwicker et al. 2001b].

There has been recent interest in *differentiable* point-based rendering techniques [Wiles et al. 2020; Yifan et al. 2019]. Points have been augmented with neural features and rendered using a CNN [Aliev et al. 2020; Rückert et al. 2022] resulting in fast or even real-time view synthesis; however they still depend on MVS for the initial geometry, and as such inherit its artifacts, most notably over- or under-reconstruction in hard cases such as featureless/shiny areas or thin structures.

Point-based α -blending and NeRF-style volumetric rendering share essentially the same image formation model. Specifically, the color C is given by volumetric rendering along a ray:

$$C = \sum_{i=1}^N T_i (1 - \exp(-\sigma_i \delta_i)) \mathbf{c}_i \quad \text{with} \quad T_i = \exp\left(-\sum_{j=1}^{i-1} \sigma_j \delta_j\right), \quad (1)$$

where samples of density σ , transmittance T , and color \mathbf{c} are taken along the ray with intervals δ_i . This can be re-written as

$$C = \sum_{i=1}^N T_i \alpha_i \mathbf{c}_i, \quad (2)$$

with

$$\alpha_i = (1 - \exp(-\sigma_i \delta_i)) \quad \text{and} \quad T_i = \prod_{j=1}^{i-1} (1 - \alpha_j).$$

A typical neural point-based approach (e.g., [Kopanas et al. 2022, 2021]) computes the color C of a pixel by blending N ordered points overlapping the pixel:

$$C = \sum_{i \in N} c_i \alpha_i \prod_{j=1}^{i-1} (1 - \alpha_j), \quad (3)$$

where \mathbf{c}_i is the color of each point and α_i is given by evaluating a 2D Gaussian with covariance Σ [Yifan et al. 2019] multiplied with a learned per-point opacity.

From Eq. 2 and Eq. 3, we can clearly see that the image formation model is the same. However, the rendering algorithm is very different. NeRFs are a continuous representation implicitly representing empty/occupied space; expensive random sampling is required to find the samples in Eq. 2 with consequent noise and computational expense. In contrast, points are an unstructured, discrete representation that is flexible enough to allow creation, destruction, and displacement of geometry similar to NeRF. This is achieved by optimizing opacity and positions, as shown by previous work [Kopanas et al. 2021], while avoiding the shortcomings of a full volumetric representation.

Pulsar [Lassner and Zollhofer 2021] achieves fast *sphere* rasterization which inspired our tile-based and sorting renderer. However, given the analysis above, we want to maintain (approximate) conventional α -blending on sorted splats to have the advantages of volumetric representations: Our rasterization respects visibility order in contrast to their order-independent method. In addition, we back-propagate gradients on all splats in a pixel and rasterize anisotropic splats. These elements all contribute to the high visual quality of our results (see Sec. 7.3). In addition, previous methods mentioned above also use CNNs for rendering, which results in temporal instability. Nonetheless, the rendering speed of Pulsar [Lassner and Zollhofer 2021] and ADOP [Rückert et al. 2022] served as motivation to develop our fast rendering solution.

While focusing on specular effects, the diffuse point-based rendering track of Neural Point Catacaustics [Kopanas et al. 2022] overcomes this temporal instability by using an MLP, but still required MVS geometry as input. The most recent method [Zhang et al. 2022] in this category does not require MVS, and also uses SH for directions; however, it can only handle scenes of one object and needs masks for initialization. While fast for small resolutions and low point counts, it is unclear how it can scale to scenes of typical datasets [Barron et al. 2022; Hedman et al. 2018; Knapitsch et al. 2017]. We use 3D Gaussians for a more flexible scene representation, avoiding the need for MVS geometry and achieving real-time rendering thanks to our tile-based rendering algorithm for the projected Gaussians.

A recent approach [Xu et al. 2022] uses points to represent a radiance field with a radial basis function approach. They employ point pruning and densification techniques during optimization, but use volumetric ray-marching and cannot achieve real-time display rates.

In the domain of human performance capture, 3D Gaussians have been used to represent captured human bodies [Rhodin et al. 2015; Stoll et al. 2011]; more recently they have been used with volumetric ray-marching for vision tasks [Wang et al. 2023]. Neural volumetric primitives have been proposed in a similar context [Lombardi et al. 2021]. While these methods inspired the choice of 3D Gaussians as our scene representation, they focus on the specific case of reconstructing and rendering a single isolated object (a human body or face), resulting in scenes with small depth complexity. In contrast, our optimization of *anisotropic* covariance, our interleaved optimization/density control, and efficient depth sorting for rendering allow us to handle complete, complex scenes including background, both indoors and outdoors and with large depth complexity.

3 OVERVIEW

The input to our method is a set of images of a **static scene**, together with the corresponding cameras calibrated by SfM [Schönberger and Frahm 2016] which produces a sparse point cloud as a side-effect. From these points we create a **set of 3D Gaussians (Sec. 4)**, **defined by a position (mean), covariance matrix and opacity α** , that **allows a very flexible optimization regime**. This results in a reasonably compact representation of the 3D scene, in part because highly **anisotropic volumetric splats** can be used to represent fine structures compactly. **The directional appearance component (color) of the radiance field is represented via spherical harmonics (SH)**, following standard practice [Fridovich-Keil and Yu et al. 2022; Müller et al. 2022]. Our algorithm proceeds to create the radiance field representation (Sec. 5) via a sequence of optimization steps of 3D Gaussian parameters, i.e., position, covariance, α and SH coefficients interleaved with operations for adaptive control of the Gaussian density. The key to the efficiency of our method is our tile-based rasterizer (Sec. 6) that allows **α -blending of anisotropic splats**, respecting visibility order thanks to fast sorting. Our fast rasterizer also includes a fast **backward pass** by tracking accumulated α values, without a limit on the **number of Gaussians that can receive gradients**. The overview of our method is illustrated in Fig. 2.

4 DIFFERENTIABLE 3D GAUSSIAN SPLATTING

Our goal is to optimize a scene representation that allows high-quality novel view synthesis, starting from a sparse set of (SfM) points without normals. To do this, we need a primitive that inherits the properties of differentiable volumetric representations, while at the same time being unstructured and explicit to allow very fast rendering. We choose **3D Gaussians, which are differentiable and can be easily projected to 2D splats allowing fast α -blending for rendering**.

Our representation has similarities to previous methods that use 2D points [Kopanas et al. 2021; Yifan et al. 2019] and assume each point is a small planar circle with a normal. Given the extreme sparsity of SfM points it is very hard to estimate normals. Similarly,

optimizing very noisy normals from such an estimation would be very challenging. Instead, we model the geometry as a set of **3D Gaussians that do not require normals**. Our Gaussians are defined by a full 3D covariance matrix Σ defined in world space [Zwicker et al. 2001a] centered at point (mean) μ :

$$G(x) = e^{-\frac{1}{2}(x)^T \Sigma^{-1}(x)} \quad (4)$$

This Gaussian is multiplied by α in our blending process.

However, we need to project our 3D Gaussians to 2D for rendering. Zwicker et al. [2001a] demonstrate how to do this projection to image space. Given a viewing transformation W the covariance matrix Σ' in camera coordinates is given as follows:

$$\Sigma' = JW \Sigma W^T J^T \quad (5)$$

where J is the **Jacobian of the affine approximation** of the projective transformation. Zwicker et al. [2001a] also show that if we skip the third row and column of Σ' , we obtain a 2×2 variance matrix with the same structure and properties as if we would start from planar points with normals, as in previous work [Kopanas et al. 2021].

An obvious approach would be to directly optimize the covariance matrix Σ to obtain 3D Gaussians that represent the radiance field. However, **covariance matrices have physical meaning only when they are positive semi-definite**. For our optimization of all our parameters, we use **gradient descent that cannot be easily constrained to produce such valid matrices**, and update steps and gradients can very easily create invalid covariance matrices.

As a result, we opted for a more intuitive, yet equivalently expressive representation for optimization. The covariance matrix Σ of a 3D Gaussian is analogous to describing the configuration of an ellipsoid. Given a scaling matrix S and rotation matrix R , we can find the corresponding Σ :

$$\Sigma = RSS^T R^T \quad (6)$$

To allow independent optimization of both factors, we store them separately: **a 3D vector s for scaling and a quaternion q to represent rotation**. These can be trivially converted to their respective matrices and combined, making sure to normalize q to obtain a valid unit quaternion.

To avoid significant overhead due to automatic differentiation during training, we derive the gradients for all parameters explicitly. Details of the exact derivative computations are in appendix A.

This representation of anisotropic covariance – suitable for optimization – allows us to optimize 3D Gaussians to adapt to the geometry of different shapes in captured scenes, resulting in a fairly compact representation. Fig. 3 illustrates such cases.

5 OPTIMIZATION WITH ADAPTIVE DENSITY CONTROL OF 3D GAUSSIANS

The core of our approach is the optimization step, which creates a dense set of 3D Gaussians accurately representing the scene for free-view synthesis. In addition to positions p , α , and covariance Σ , we also optimize SH coefficients representing color c of each Gaussian to correctly capture the view-dependent appearance of the scene. The optimization of these parameters is interleaved with steps that control the density of the Gaussians to better represent the scene.

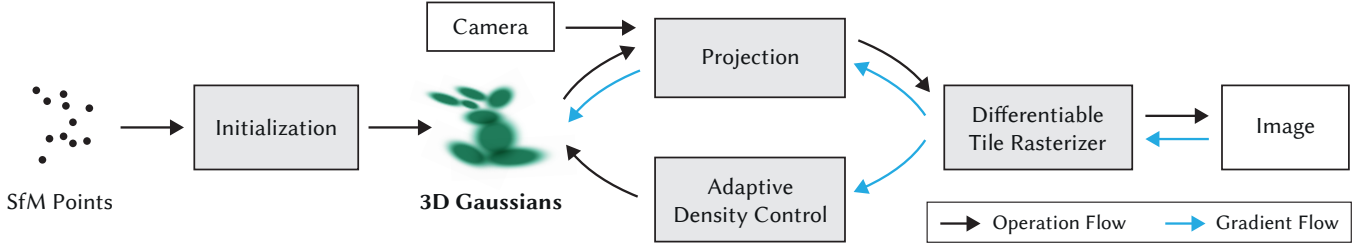


Fig. 2. Optimization starts with the sparse SfM point cloud and creates a set of 3D Gaussians. We then optimize and adaptively control the density of this set of Gaussians. During optimization we use our fast tile-based renderer, allowing competitive training times compared to SOTA fast radiance field methods. Once trained, our renderer allows real-time navigation for a wide variety of scenes.



Fig. 3. We visualize the 3D Gaussians after optimization by shrinking them 60% (far right). This clearly shows the anisotropic shapes of the 3D Gaussians that compactly represent complex geometry after optimization. Left the actual rendered image.

5.1 Optimization

The optimization is based on successive iterations of rendering and comparing the resulting image to the training views in the captured dataset. Inevitably, geometry may be incorrectly placed due to the ambiguities of 3D to 2D projection. Our optimization thus needs to be able to *create* geometry and also *destroy* or *move* geometry if it has been incorrectly positioned. The quality of the parameters of the covariances of the 3D Gaussians is critical for the compactness of the representation since **large homogeneous areas** can be captured with a small number of large anisotropic Gaussians.

We use Stochastic Gradient Descent techniques for optimization, taking full advantage of standard GPU-accelerated frameworks, and the ability to add custom CUDA kernels for some operations, following recent best practice [Fridovich-Keil and Yu et al. 2022; Sun et al. 2022]. In particular, our fast rasterization (see Sec. 6) is critical in the efficiency of our optimization, since it is the main computational bottleneck of the optimization.

We use a sigmoid activation function for α to constrain it in the $[0 - 1]$ range and obtain smooth gradients, and an exponential activation function for the scale of the covariance for similar reasons.

We estimate the initial covariance matrix as an isotropic Gaussian with axes equal to the mean of the distance to the closest three points. We use a standard exponential decay scheduling technique similar to PlenoXels [Fridovich-Keil and Yu et al. 2022], but for positions only. The loss function is \mathcal{L}_1 combined with a D-SSIM term:

$$\mathcal{L} = (1 - \lambda)\mathcal{L}_1 + \lambda\mathcal{L}_{\text{D-SSIM}} \quad (7)$$

We use $\lambda = 0.2$ in all our tests. We provide details of the learning schedule and other elements in Sec. 7.1.

5.2 Adaptive Control of Gaussians

We start with the initial set of sparse points from SfM and then apply our method to adaptively control the number of Gaussians and their density over unit volume¹, allowing us to go from an initial sparse set of Gaussians to a denser set that better represents the scene, and with correct parameters. After optimization warm-up (see Sec. 7.1), we densify every 100 iterations and remove any Gaussians that are essentially transparent, i.e., with α less than a threshold ϵ_α .

Our adaptive control of the Gaussians needs to populate empty areas. It focuses on regions with missing geometric features (“under-reconstruction”), but also in regions where Gaussians cover large areas in the scene (which often correspond to “over-reconstruction”). We observe that both have *large* view-space positional gradients. Intuitively, this is likely because they correspond to regions that are not yet well reconstructed, and the optimization tries to move the Gaussians to correct this.

Since both cases are good candidates for densification, we densify Gaussians with an average magnitude of view-space position gradients above a threshold τ_{pos} , which we set to 0.0002 in our tests.

We next present details of this process, illustrated in Fig. 4.

For small Gaussians that are in under-reconstructed regions, we need to cover the new geometry that must be created. For this, it is preferable to clone the Gaussians, by simply creating a copy of the same size, and moving it in the direction of the positional gradient.

On the other hand, large Gaussians in regions with high variance need to be split into smaller Gaussians. We replace such Gaussians by two new ones, and divide their scale by a factor of $\phi = 1.6$ which we determined experimentally. We also initialize their position by using the original 3D Gaussian as a PDF for sampling.

In the first case we detect and treat the need for increasing both the total volume of the system and the number of Gaussians, while in the second case we conserve total volume but increase the number of Gaussians. Similar to other volumetric representations, our optimization can get stuck with floaters close to the input cameras; in our case this may result in an unjustified increase in the Gaussian density. An effective way to moderate the increase in the number of Gaussians is to set the α value close to zero every $N = 3000$

¹Density of Gaussians should not be confused of course with density σ in the NeRF literature.

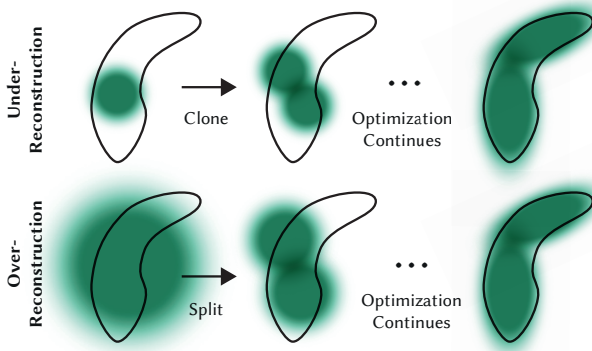


Fig. 4. Our adaptive Gaussian densification scheme. *Top row (under-reconstruction)*: When small-scale geometry (black outline) is insufficiently covered, we clone the respective Gaussian. *Bottom row (over-reconstruction)*: If small-scale geometry is represented by one large splat, we split it in two.

iterations. The optimization then increases the α for the Gaussians where this is needed while allowing our culling approach to remove Gaussians with α less than ϵ_α as described above. Gaussians may shrink or grow and considerably overlap with others, but we periodically remove Gaussians that are very large in worldspace and those that have a big footprint in viewspace. This strategy results in overall good control over the total number of Gaussians. The Gaussians in our model remain primitives in Euclidean space at all times; unlike other methods [Barron et al. 2022; Fridovich-Keil and Yu et al. 2022], we do not require space compaction, warping or projection strategies for distant or large Gaussians.

6 FAST DIFFERENTIABLE RASTERIZER FOR GAUSSIANS

Our goals are to have fast overall rendering and fast sorting to allow approximate α -blending – including for anisotropic splats – and to avoid hard limits on the number of splats that can receive gradients that exist in previous work [Lassner and Zollhofer 2021].

To achieve these goals, we design a tile-based rasterizer for Gaussian splats inspired by recent software rasterization approaches [Lassner and Zollhofer 2021] to pre-sort primitives for an entire image at a time, avoiding the expense of sorting per pixel that hindered previous α -blending solutions [Kopanas et al. 2022, 2021]. Our fast rasterizer allows efficient backpropagation over an arbitrary number of blended Gaussians with low additional memory consumption, requiring only a constant overhead per pixel. Our rasterization pipeline is fully differentiable, and given the projection to 2D (Sec. 4) can rasterize anisotropic splats similar to previous 2D splatting methods [Kopanas et al. 2021].

Our method starts by splitting the screen into 16×16 tiles, and then proceeds to cull 3D Gaussians against the view frustum and each tile. Specifically, we only keep Gaussians with a 99% confidence interval intersecting the view frustum. Additionally, we use a guard band to trivially reject Gaussians at extreme positions (i.e., those with means close to the near plane and far outside the view frustum), since computing their projected 2D covariance would be unstable. We then instantiate each Gaussian according to the

number of tiles they overlap and assign each instance a key that combines view space depth and tile ID. We then sort Gaussians based on these keys using a single fast GPU Radix sort [Merrill and Grimshaw 2010]. Note that there is no additional per-pixel ordering of points, and blending is performed based on this initial sorting. As a consequence, our α -blending can be approximate in some configurations. However, these approximations become negligible as splats approach the size of individual pixels. We found that this choice greatly enhances training and rendering performance without producing visible artifacts in converged scenes.

After sorting Gaussians, we produce a list for each tile by identifying the first and last depth-sorted entry that splats to a given tile. For rasterization, we launch one thread block for each tile. Each block first collaboratively loads packets of Gaussians into shared memory and then, for a given pixel, accumulates color and α values by traversing the lists front-to-back, thus maximizing the gain in parallelism both for data loading/sharing and processing. When we reach a target saturation of α in a pixel, the corresponding thread stops. At regular intervals, threads in a tile are queried and the processing of the entire tile terminates when all pixels have saturated (i.e., α goes to 1). Details of sorting and a high-level overview of the overall rasterization approach are given in Appendix C.

During rasterization, the saturation of α is the only stopping criterion. In contrast to previous work, we do not limit the number of blended primitives that receive gradient updates. We enforce this property to allow our approach to handle scenes with an arbitrary, varying depth complexity and accurately learn them, without having to resort to scene-specific hyperparameter tuning. During the backward pass, we must therefore recover the full sequence of blended points per-pixel in the forward pass. One solution would be to store arbitrarily long lists of blended points per-pixel in global memory [Kopanas et al. 2021]. To avoid the implied dynamic memory management overhead, we instead choose to traverse the per-tile lists again; we can reuse the sorted array of Gaussians and tile ranges from the forward pass. To facilitate gradient computation, we now traverse them back-to-front.

The traversal starts from the last point that affected any pixel in the tile, and loading of points into shared memory again happens collaboratively. Additionally, each pixel will only start (expensive) overlap testing and processing of points if their depth is lower than or equal to the depth of the last point that contributed to its color during the forward pass. Computation of the gradients described in Sec. 4 requires the accumulated opacity values at each step during the original blending process. Rather than traversing an explicit list of progressively shrinking opacities in the backward pass, we can recover these intermediate opacities by storing only the total accumulated opacity at the end of the forward pass. Specifically, each point stores the final accumulated opacity α in the forward process; we divide this by each point's α in our back-to-front traversal to obtain the required coefficients for gradient computation.

7 IMPLEMENTATION, RESULTS AND EVALUATION

We next discuss some details of implementation, present results and the evaluation of our algorithm compared to previous work and ablation studies.

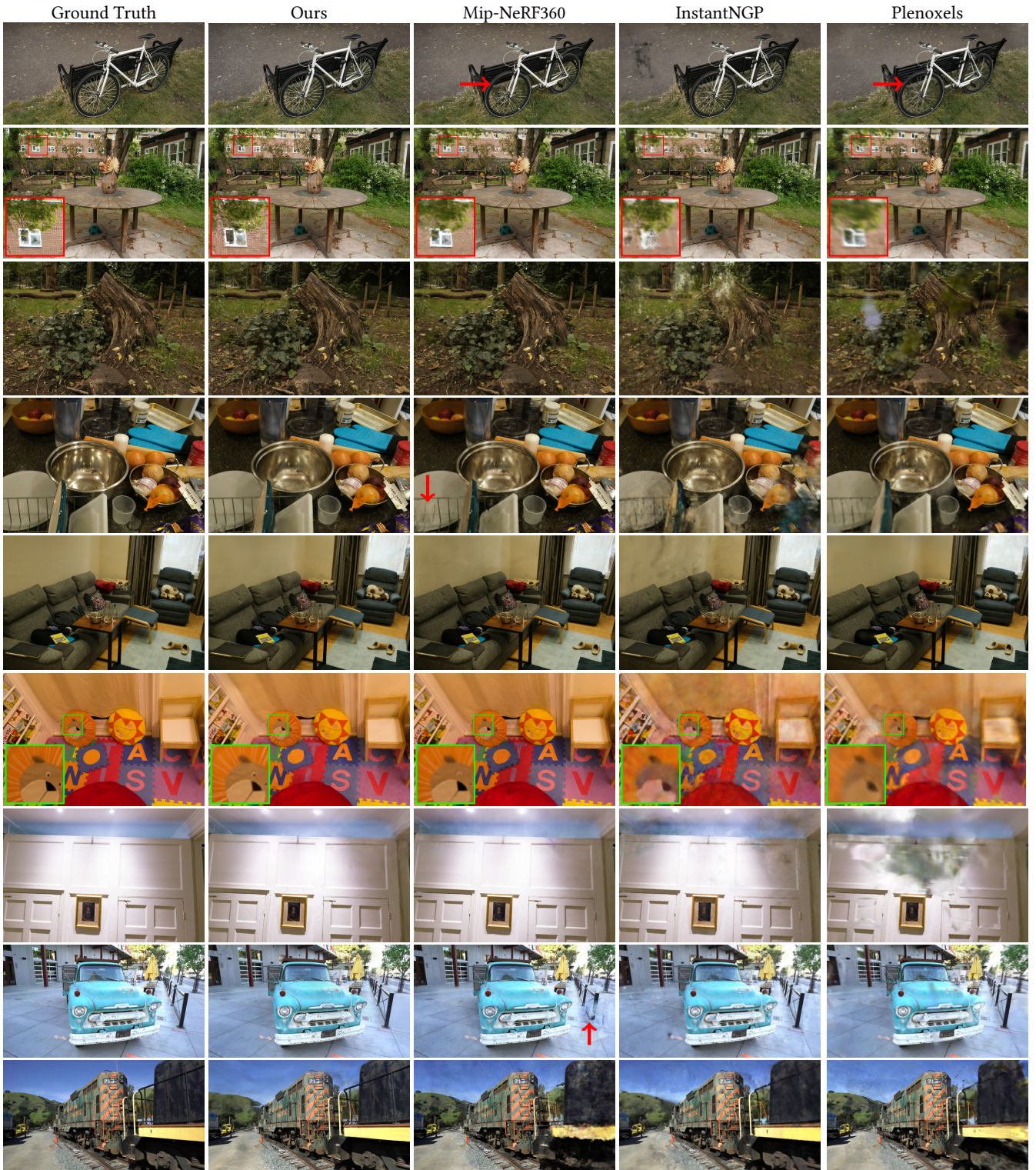


Fig. 5. We show comparisons of ours to previous methods and the corresponding ground truth images from held-out test views. The scenes are, from the top down: BICYCLE, GARDEN, STUMP, COUNTER and Room from the Mip-NeRF360 dataset; PLAYROOM, DRJOHNSON from the Deep Blending dataset [Hedman et al. 2018] and TRUCK and TRAIN from Tanks&Temples. Non-obvious differences in quality highlighted by arrows/insets.

Table 1. Quantitative evaluation of our method compared to previous work, computed over three datasets. Results marked with dagger \dagger have been directly adopted from the original paper, all others were obtained in our own experiments.

Dataset Method Metric	Mip-NeRF360						Tanks&Temples						Deep Blending					
	SSIM \uparrow	PSNR \uparrow	LPIPS \downarrow	Train	FPS	Mem	SSIM \uparrow	PSNR \uparrow	LPIPS \downarrow	Train	FPS	Mem	SSIM \uparrow	PSNR \uparrow	LPIPS \downarrow	Train	FPS	Mem
Plenoxels	0.626	23.08	0.463	25m49s	6.79	2.1GB	0.719	21.08	0.379	25m5s	13.0	2.3GB	0.795	23.06	0.510	27m49s	11.2	2.7GB
INGP-Base	0.671	25.30	0.371	5m37s	11.7	13MB	0.723	21.72	0.330	5m26s	17.1	13MB	0.797	23.62	0.423	6m31s	3.26	13MB
INGP-Big	0.699	25.59	0.331	7m30s	9.43	48MB	0.745	21.92	0.305	6m59s	14.4	48MB	0.817	24.96	0.390	8m	2.79	48MB
M-NeRF360	0.792 \dagger	27.69 \dagger	0.237 \dagger	48h	0.06	8.6MB	0.759	22.22	0.257	48h	0.14	8.6MB	0.901	29.40	0.245	48h	0.09	8.6MB
Ours-7K	0.770	25.60	0.279	6m25s	160	523MB	0.767	21.20	0.280	6m55s	197	270MB	0.875	27.78	0.317	4m35s	172	386MB
Ours-30K	0.815	27.21	0.214	41m33s	134	734MB	0.841	23.14	0.183	26m54s	154	411MB	0.903	29.41	0.243	36m2s	137	676MB



Fig. 6. For some scenes (above) we can see that even at 7K iterations ($\sim 5\text{min}$ for this scene), our method has captured the train quite well. At 30K iterations ($\sim 35\text{min}$) the background artifacts have been reduced significantly. For other scenes (below), the difference is barely visible; 7K iterations ($\sim 8\text{min}$) is already very high quality.

Table 2. PSNR scores for Synthetic NeRF, we start with 100K randomly initialized points. Competing metrics extracted from respective papers.

	Mic	Chair	Ship	Materials	Lego	Drums	Ficus	Hotdog	Avg.
Plenoxels	33.26	33.98	29.62	29.14	34.10	25.35	31.83	36.81	31.76
INGP-Base	36.22	35.00	31.10	29.78	36.39	26.02	33.51	37.40	33.18
Mip-NeRF	36.51	35.14	30.41	30.71	35.70	25.48	33.29	37.48	33.09
Point-NeRF	35.95	35.40	30.97	29.61	35.04	26.06	36.13	37.30	33.30
Ours-30K	35.36	35.83	30.80	30.00	35.78	26.15	34.87	37.72	33.32

7.1 Implementation

We implemented our method in Python using the PyTorch framework and wrote custom CUDA kernels for rasterization that are extended versions of previous methods [Kopanas et al. 2021], and use the NVIDIA CUB sorting routines for the fast Radix sort [Merrill and Grimshaw 2010]. We also built an interactive viewer using the open-source SIBR [Bonopera et al. 2020], used for interactive viewing. We used this implementation to measure our achieved frame rates. The source code and all our data are available at: <https://repo-sam.inria.fr/fungraph/3d-gaussian-splatting/>

Optimization Details. For stability, we “warm-up” the computation in lower resolution. Specifically, we start the optimization using 4 times smaller image resolution and we upsample twice after 250 and 500 iterations.

SH coefficient optimization is sensitive to the lack of angular information. For typical “NeRF-like” captures where a central object

is observed by photos taken in the entire hemisphere around it, the optimization works well. However, if the capture has angular regions missing (e.g., when capturing the corner of a scene, or performing an “inside-out” [Hedman et al. 2016] capture) completely incorrect values for the zero-order component of the SH (i.e., the base or diffuse color) can be produced by the optimization. To overcome this problem we start by optimizing only the zero-order component, and then introduce one band of the SH after every 1000 iterations until all 4 bands of SH are represented.

7.2 Results and Evaluation

Results. We tested our algorithm on a total of 13 real scenes taken from previously published datasets and the synthetic Blender dataset [Mildenhall et al. 2020]. In particular, we tested our approach on the full set of scenes presented in Mip-Nerf360 [Barron et al. 2022], which is the current state of the art in NeRF rendering quality, two scenes from the Tanks&Temples dataset [2017] and two scenes provided by Hedman et al. [Hedman et al. 2018]. The scenes we chose have very different capture styles, and cover both bounded indoor scenes and large unbounded outdoor environments. We use the same hyperparameter configuration for all experiments in our evaluation. All results are reported running on an A6000 GPU, except for the Mip-Nerf360 method (see below).

In supplemental, we show a rendered video path for a selection of scenes that contain views far from the input photos.

Real-World Scenes. In terms of quality, the current state-of-the-art is Mip-Nerf360 [Barron et al. 2021]. We compare against this method as a quality benchmark. We also compare against two of the most recent fast NeRF methods: InstantNGP [Müller et al. 2022] and Plenoxels [Fridovich-Keil and Yu et al. 2022].

We use a train/test split for datasets, using the methodology suggested by Mip-Nerf360, taking every 8th photo for test, for consistent and meaningful comparisons to generate the error metrics, using the standard PSNR, L-PIPS, and SSIM metrics used most frequently in the literature; please see Table 1. All numbers in the table are from our own runs of the author’s code for all previous methods, except for those of Mip-Nerf360 on their dataset, in which we copied the numbers from the original publication to avoid confusion about the current SOTA. For the images in our figures, we used our own run of Mip-Nerf360: the numbers for these runs are in Appendix D. We also show the average training time, rendering speed, and memory used to store optimized parameters. We report results for a basic configuration of InstantNGP (Base) that run for 35K iterations as well as a slightly larger network suggested by the authors (Big), and two configurations, 7K and 30K iterations for ours. We show

Table 3. PSNR Score for ablation runs. For this experiment, we manually downsampled high-resolution versions of each scene’s input images to the established rendering resolution of our other experiments. Doing so reduces random artifacts (e.g., due to JPEG compression in the pre-downscaled Mip-NeRF360 inputs).

	Truck-5K	Garden-5K	Bicycle-5K	Truck-30K	Garden-30K	Bicycle-30K	Average-5K	Average-30K
Limited-BW	14.66	22.07	20.77	13.84	22.88	20.87	19.16	19.19
Random Init	16.75	20.90	19.86	18.02	22.19	21.05	19.17	20.42
No-Split	18.31	23.98	22.21	20.59	26.11	25.02	21.50	23.90
No-SH	22.36	25.22	22.88	24.39	26.59	25.08	23.48	25.35
No-Clone	22.29	25.61	22.15	24.82	27.47	25.46	23.35	25.91
Isotropic	22.40	25.49	22.81	23.89	27.00	24.81	23.56	25.23
Full	22.71	25.82	23.18	24.81	27.70	25.65	23.90	26.05

the difference in visual quality for our two configurations in Fig. 6. In many cases, quality at 7K iterations is already quite good.

The training times vary over datasets and we report them separately. Note that image resolutions also vary over datasets. In the project website, we provide all the renders of test views we used to compute the statistics for all the methods (ours and previous work) on all scenes. Note that we kept the native input resolution for all renders.

The table shows that our fully converged model achieves quality that is on par and sometimes slightly better than the SOTA Mip-NeRF360 method; note that on the same hardware, their average training time was 48 hours², compared to our 35–45min, and their rendering time is 10s/frame. We achieve comparable quality to InstantNGP and Plenoxels after 5–10m of training, but additional training time allows us to achieve SOTA quality which is not the case for the other fast methods. For Tanks & Temples, we achieve similar quality as the basic InstantNGP at a similar training time (~7min in our case).

We also show visual results of this comparison for a left-out test view for ours and the previous rendering methods selected for comparison in Fig. 5; the results of our method are for 30K iterations of training. We see that in some cases even Mip-NeRF360 has remaining artifacts that our method avoids (e.g., blurriness in vegetation – in BICYCLE, STUMP – or on the walls in ROOM). In the supplemental video and web page we provide comparisons of paths from a distance. Our method tends to preserve visual detail of well-covered regions even from far away, which is not always the case for previous methods.

Synthetic Bounded Scenes. In addition to realistic scenes, we also evaluate our approach on the synthetic *Blender* dataset [Mildenhall et al. 2020]. The scenes in question provide an exhaustive set of views, are limited in size, and provide exact camera parameters. In such scenarios, we can achieve state-of-the-art results even with random initialization: we start training from 100K uniformly random Gaussians inside a volume that encloses the scene bounds. Our approach quickly and automatically prunes them to about 6–10K meaningful Gaussians. The final size of the trained model after 30K iterations reaches about 200–500K Gaussians per scene. We report and compare our achieved PSNR scores with previous methods in Table 2 using a white background for compatibility. Examples can

²We trained Mip-NeRF360 on a 4-GPU A100 node for 12 hours, equivalent to 48 hours on a single GPU. Note that A100’s are faster than A6000 GPUs.

be seen in Fig. 10 (second image from the left) and in supplemental material. The trained synthetic scenes rendered at 180–300 FPS.

Compactness. In comparison to previous explicit scene representations, the anisotropic Gaussians used in our optimization are capable of modelling complex shapes with a lower number of parameters. We showcase this by evaluating our approach against the highly compact, point-based models obtained by [Zhang et al. 2022]. We start from their initial point cloud which is obtained by space carving with foreground masks and optimize until we break even with their reported PSNR scores. This usually happens within 2–4 minutes. We surpass their reported metrics using approximately one-fourth of their point count, resulting in an average model size of 3.8 MB, as opposed to their 9 MB. We note that for this experiment, we only used two degrees of our spherical harmonics, similar to theirs.

7.3 Ablations

We isolated the different contributions and algorithmic choices we made and constructed a set of experiments to measure their effect. Specifically we test the following aspects of our algorithm: initialization from SfM, our densification strategies, anisotropic covariance, the fact that we allow an unlimited number of splats to have gradients and use of spherical harmonics. The quantitative effect of each choice is summarized in Table 3.

Initialization from SfM. We also assess the importance of initializing the 3D Gaussians from the SfM point cloud. For this ablation, we uniformly sample a cube with a size equal to three times the extent of the input camera’s bounding box. We observe that our method performs relatively well, avoiding complete failure even without the SfM points. Instead, it degrades mainly in the background, see Fig. 7. Also in areas not well covered from training views, the random initialization method appears to have more floaters that cannot be removed by optimization. On the other hand, the synthetic NeRF dataset does not have this behavior because it has no background and is well constrained by the input cameras (see discussion above).

Densification. We next evaluate our two densification methods, more specifically the clone and split strategy described in Sec. 5. We disable each method separately and optimize using the rest of the method unchanged. Results show that splitting big Gaussians is important to allow good reconstruction of the background as seen in Fig. 8, while cloning the small Gaussians instead of splitting them allows for a better and faster convergence especially when thin structures appear in the scene.



Fig. 7. Initialization with SfM points helps. Above: initialization with a random point cloud. Below: initialization using SfM points.



Fig. 8. Ablation of densification strategy for the two cases "clone" and "split" (Sec. 5).

Unlimited depth complexity of splats with gradients. We evaluate if skipping the gradient computation after the N front-most points



Fig. 9. If we limit the number of points that receive gradients, the effect on visual quality is significant. Left: limit of 10 Gaussians that receive gradients. Right: our full method.

will give us speed without sacrificing quality, as suggested in Pulsar [Lassner and Zollhofer 2021]. In this test, we choose $N=10$, which is two times higher than the default value in Pulsar, but it led to unstable optimization because of the severe approximation in the gradient computation. For the TRUCK scene, quality degraded by 11dB in PSNR (see Table 3, Limited-BW), and the visual outcome is shown in Fig. 9 for GARDEN.

Anisotropic Covariance. An important algorithmic choice in our method is the optimization of the full covariance matrix for the 3D Gaussians. To demonstrate the effect of this choice, we perform an ablation where we remove anisotropy by optimizing a single scalar value that controls the radius of the 3D Gaussian on all three axes. The results of this optimization are presented visually in Fig. 10. We observe that the anisotropy significantly improves the quality of the 3D Gaussian's ability to align with surfaces, which in turn allows for much higher rendering quality while maintaining the same number of points.

Spherical Harmonics. Finally, the use of spherical harmonics improves our overall PSNR scores since they compensate for the view-dependent effects (Table 3).

7.4 Limitations

Our method is not without limitations. In regions where the scene is not well observed we have artifacts; in such regions, other methods also struggle (e.g., Mip-NeRF360 in Fig. 11). Even though the anisotropic Gaussians have many advantages as described above, our method can create elongated artifacts or "splotchy" Gaussians (see Fig. 12); again previous methods also struggle in these cases.

We also occasionally have popping artifacts when our optimization creates large Gaussians; this tends to happen in regions with view-dependent appearance. One reason for these popping artifacts is the trivial rejection of Gaussians via a guard band in the rasterizer. A more principled culling approach would alleviate these artifacts. Another factor is our simple visibility algorithm, which can lead to Gaussians suddenly switching depth/blending order. This could be addressed by antialiasing, which we leave as future work. Also, we currently do not apply any regularization to our optimization; doing so would help with both the unseen region and popping artifacts.

While we used the same hyperparameters for our full evaluation, early experiments show that reducing the position learning rate can be necessary to converge in very large scenes (e.g., urban datasets).



Fig. 10. We train scenes with Gaussian anisotropy disabled and enabled. The use of anisotropic volumetric splats enables modelling of fine structures and has a significant impact on visual quality. Note that for illustrative purposes, we restricted Ficus to use no more than 5k Gaussians in both configurations.

Even though we are very compact compared to previous point-based approaches, our memory consumption is significantly higher than NeRF-based solutions. During training of large scenes, peak GPU memory consumption can exceed 20 GB in our unoptimized prototype. However, this figure could be significantly reduced by a careful low-level implementation of the optimization logic (similar to InstantNGP). Rendering the trained scene requires sufficient GPU memory to store the full model (several hundred megabytes for large-scale scenes) and an additional 30–500 MB for the rasterizer, depending on scene size and image resolution. We note that there are many opportunities to further reduce memory consumption of our method. Compression techniques for point clouds is a well-studied field [De Queiroz and Chou 2016]; it would be interesting to see how such approaches could be adapted to our representation.



Fig. 11. Comparison of failure artifacts: Mip-NeRF360 has “floaters” and grainy appearance (left, foreground), while our method produces coarse, anisotropic Gaussians resulting in low-detail visuals (right, background). TRAIN scene.



Fig. 12. In views that have little overlap with those seen during training, our method may produce artifacts (right). Again, Mip-NeRF360 also has artifacts in these cases (left). DRJOHNSON scene.

8 DISCUSSION AND CONCLUSIONS

We have presented the first approach that truly allows real-time, high-quality radiance field rendering, in a wide variety of scenes and capture styles, while requiring training times competitive with the fastest previous methods.

Our choice of a 3D Gaussian primitive preserves properties of volumetric rendering for optimization while directly allowing fast splat-based rasterization. Our work demonstrates that – contrary to widely accepted opinion – a continuous representation is *not* strictly necessary to allow fast and high-quality radiance field training.

The majority (~80%) of our training time is spent in Python code, since we built our solution in PyTorch to allow our method to be easily used by others. Only the rasterization routine is implemented as optimized CUDA kernels. We expect that porting the remaining optimization entirely to CUDA, as e.g., done in InstantNGP [Müller et al. 2022], could enable significant further speedup for applications where performance is essential.

We also demonstrated the importance of building on real-time rendering principles, exploiting the power of the GPU and speed of software rasterization pipeline architecture. These design choices are the key to performance both for training and real-time rendering, providing a competitive edge in performance over previous volumetric ray-marching.

It would be interesting to see if our Gaussians can be used to perform mesh reconstructions of the captured scene. Aside from practical implications given the widespread use of meshes, this would allow us to better understand where our method stands exactly in the continuum between volumetric and surface representations.

In conclusion, we have presented the first real-time rendering solution for radiance fields, with rendering quality that matches the best expensive previous methods, with training times competitive with the fastest existing solutions.

ACKNOWLEDGMENTS

This research was funded by the ERC Advanced grant FUNGRAPH No 788065 <http://fungraph.inria.fr>. The authors are grateful to Adobe for generous donations, the OPAL infrastructure from Université Côte d’Azur and for the HPC resources from GENCI-IDRIS (Grant 2022-AD011013409). The authors thank the anonymous reviewers for their valuable feedback, P. Hedman and A. Tewari for proofreading earlier drafts also T. Müller, A. Yu and S. Fridovich-Keil for helping with the comparisons.

REFERENCES

- Kara-Ali Aliev, Artem Sevastopolsky, Maria Kolos, Dmitry Ulyanov, and Victor Lempitsky. 2020. Neural Point-Based Graphics. In *Computer Vision – ECCV 2020: 16th European Conference, Glasgow, UK, August 23–28, 2020, Proceedings, Part XXII*. 696–712.
- Jonathan T Barron, Ben Mildenhall, Matthew Tancik, Peter Hedman, Ricardo Martin-Brualla, and Pratul P Srinivasan. 2021. Mip-nerf: A multiscale representation for anti-aliasing neural radiance fields. In *Proceedings of the IEEE/CVF International Conference on Computer Vision*. 5855–5864.
- Jonathan T. Barron, Ben Mildenhall, Dor Verbin, Pratul P. Srinivasan, and Peter Hedman. 2022. Mip-NeRF 360: Unbounded Anti-Aliased Neural Radiance Fields. *CVPR* (2022).
- Sebastien Bonopera, Jerome Esnault, Siddhant Prakash, Simon Rodriguez, Theo Thonat, Mehdi Benadel, Gaurav Chaurasia, Julien Philip, and George Drettakis. 2020. sibr: A System for Image Based Rendering. https://gitlab.inria.fr/sibr/sibr_core
- Mario Botsch, Alexander Hornung, Matthias Zwicker, and Leif Kobbelt. 2005. High-Quality Surface Splatting on Today's GPUs. In *Proceedings of the Second Eurographics / IEEE VGTC Conference on Point-Based Graphics* (New York, USA) (SPBG'05). Eurographics Association, Goslar, DEU, 17–24.
- Chris Buehler, Michael Bosse, Leonard McMillan, Steven Gortler, and Michael Cohen. 2001. Unstructured lumigraph rendering. In *Proc. SIGGRAPH*.
- Gaurav Chaurasia, Sylvain Duchene, Olga Sorkine-Hornung, and George Drettakis. 2013. Depth synthesis and local warps for plausible image-based navigation. *ACM Transactions on Graphics (TOG)* 32, 3 (2013), 1–12.
- Anpei Chen, Zexiang Xu, Andreas Geiger, Jingyu Yu, and Hao Su. 2022b. TensorRF: Tensorial Radiance Fields. In *European Conference on Computer Vision (ECCV)*.
- Zhiqin Chen, Thomas Funkhouser, Peter Hedman, and Andrea Tagliasacchi. 2022a. MobileNeRF: Exploiting the Polygon Rasterization Pipeline for Efficient Neural Field Rendering on Mobile Architectures. *arXiv preprint arXiv:2208.00277* (2022).
- Ricardo L De Queiroz and Philip A Chou. 2016. Compression of 3D point clouds using a region-adaptive hierarchical transform. *IEEE Transactions on Image Processing* 25, 8 (2016), 3947–3956.
- Martin Eisemann, Bert De Decker, Marcus Magnor, Philippe Bekaert, Edilson De Aguiar, Naveed Ahmed, Christian Theobalt, and Anita Sellent. 2008. Floating textures. In *Computer graphics forum*, Vol. 27. Wiley Online Library, 409–418.
- John Flynn, Ivan Neulander, James Philbin, and Noah Snavely. 2016. Deepstereo: Learning to predict new views from the world's imagery. In *CVPR*.
- Fridovich-Keil and Yu, Matthew Tancik, Qinhong Chen, Benjamin Recht, and Angjoo Kanazawa. 2022. Plenoxels: Radiance Fields without Neural Networks. In *CVPR*.
- Stephan J. Garbin, Marek Kowalski, Matthew Johnson, Jamie Shotton, and Julian Valentin. 2021. FastNeRF: High-Fidelity Neural Rendering at 200FPS. In *Proceedings of the IEEE/CVF International Conference on Computer Vision (ICCV)*. 14346–14355.
- Michael Goesele, Noah Snavely, Brian Curless, Hugues Hoppe, and Steven M Seitz. 2007. Multi-view stereo for community photo collections. In *ICCV*.
- Steven J Gortler, Radek Grzeszczuk, Richard Szeliski, and Michael F Cohen. 1996. The lumigraph. In *Proceedings of the 23rd annual conference on Computer graphics and interactive techniques*. 43–54.
- Markus Gross and Hanspeter Pfister. 2011. *Point-based graphics*. Elsevier.
- Jeff P. Grossman and William J. Daly. 1998. Point Sample Rendering. In *Rendering Techniques*.
- Peter Hedman, Julien Philip, True Price, Jan-Michael Frahm, George Drettakis, and Gabriel Brostow. 2018. Deep blending for free-viewpoint image-based rendering. *ACM Trans. on Graphics (TOG)* 37, 6 (2018).
- Peter Hedman, Tobias Ritschel, George Drettakis, and Gabriel Brostow. 2016. Scalable Inside-Out Image-Based Rendering. *ACM Transactions on Graphics (SIGGRAPH Asia Conference Proceedings)* 35, 6 (December 2016). <http://www-sop.inria.fr/reves/Basilic/2016/HRDB16>
- Peter Hedman, Pratul P. Srinivasan, Ben Mildenhall, Jonathan T. Barron, and Paul Debevec. 2021. Baking Neural Radiance Fields for Real-Time View Synthesis. *ICCV* (2021).
- Philipp Henzler, Niloy J Mitra, and Tobias Ritschel. 2019. Escaping plato's cave: 3d shape from adversarial rendering. In *Proceedings of the IEEE/CVF International Conference on Computer Vision*. 9984–9993.
- Arno Knapitsch, Jaesik Park, Qian-Yi Zhou, and Vladlen Koltun. 2017. Tanks and temples: Benchmarking large-scale scene reconstruction. *ACM Transactions on Graphics (ToG)* 36, 4 (2017), 1–13.
- Georgios Kopanas, Thomas Leimkühler, Gilles Rainer, Clément Jambon, and George Drettakis. 2022. Neural Point Catacaustics for Novel-View Synthesis of Reflections. *ACM Transactions on Graphics (SIGGRAPH Asia Conference Proceedings)* 41, 6 (2022), 201. <http://www-sop.inria.fr/reves/Basilic/2022/KLRJD22>
- Georgios Kopanas, Julien Philip, Thomas Leimkühler, and George Drettakis. 2021. Point-Based Neural Rendering with Per-View Optimization. *Computer Graphics Forum* 40, 4 (2021), 29–43. <https://doi.org/10.1111/cgf.14339>
- Samuli Laine and Tero Karrais. 2011. High-performance software rasterization on GPUs. In *Proceedings of the ACM SIGGRAPH Symposium on High Performance Graphics*. 79–88.
- Christoph Lassner and Michael Zollhofer. 2021. Pulsar: Efficient Sphere-Based Neural Rendering. In *Proceedings of the IEEE/CVF Conference on Computer Vision and Pattern Recognition (CVPR)*. 1440–1449.
- Marc Levoy and Pat Hanrahan. 1996. Light field rendering. In *Proceedings of the 23rd annual conference on Computer graphics and interactive techniques*. 31–42.
- Stephen Lombardi, Tomas Simon, Gabriel Schwartz, Michael Zollhofer, Yaser Sheikh, and Jason Saragih. 2021. Mixture of volumetric primitives for efficient neural rendering. *ACM Transactions on Graphics (TOG)* 40, 4 (2021), 1–13.
- Duane G Merrill and Andrew S Grimshaw. 2010. Revisiting sorting for GPGPU stream architectures. In *Proceedings of the 19th international conference on Parallel architectures and compilation techniques*. 545–546.
- Ben Mildenhall, Pratul P. Srinivasan, Matthew Tancik, Jonathan T. Barron, Ravi Ramamoorthi, and Ren Ng. 2020. NeRF: Representing Scenes as Neural Radiance Fields for View Synthesis. In *ECCV*.
- Thomas Müller, Alex Evans, Christoph Schied, and Alexander Keller. 2022. Instant Neural Graphics Primitives with a Multiresolution Hash Encoding. *ACM Trans. Graph.* 41, 4, Article 102 (July 2022), 15 pages. <https://doi.org/10.1145/3528223.3530127>
- Eric Pennen and Li Zhang. 2017. Soft 3D reconstruction for view synthesis. *ACM Transactions on Graphics (TOG)* 36, 6 (2017), 1–11.
- Hanspeter Pfister, Matthias Zwicker, Jeroen van Baar, and Markus Gross. 2000. Surfels: Surface Elements as Rendering Primitives. In *Proceedings of the 27th Annual Conference on Computer Graphics and Interactive Techniques (SIGGRAPH '00)*. ACM Press/Addison-Wesley Publishing Co., USA, 335–342. <https://doi.org/10.1145/344779.344936>
- Christian Reiser, Songyou Peng, Yiyi Liao, and Andreas Geiger. 2021. KiloNeRF: Speeding up Neural Radiance Fields with Thousands of Tiny MLPs. In *International Conference on Computer Vision (ICCV)*.
- Liu Ren, Hanspeter Pfister, and Matthias Zwicker. 2002. Object Space EWA Surface Splatting: A Hardware Accelerated Approach to High Quality Point Rendering. *Computer Graphics Forum* 21 (2002).
- Helge Rhodin, Nadia Robertini, Christian Richardt, Hans-Peter Seidel, and Christian Theobalt. 2015. A versatile scene model with differentiable visibility applied to generative pose estimation. In *Proceedings of the IEEE International Conference on Computer Vision*. 765–773.
- Gernot Riegler and Vladlen Koltun. 2020. Free view synthesis. In *European Conference on Computer Vision*. Springer, 623–640.
- Darius Rückert, Linus Franke, and Marc Stamminger. 2022. ADOP: Approximate Differentiable One-Pixel Point Rendering. *ACM Trans. Graph.* 41, 4, Article 99 (Jul 2022), 14 pages. <https://doi.org/10.1145/3528223.3530122>
- Miguel Sainz and Renato Pajarola. 2004. Point-based rendering techniques. *Computers and Graphics* 28, 6 (2004), 869–879. <https://doi.org/10.1016/j.cag.2004.08.014>
- Johannes Lutz Schönberger and Jan-Michael Frahm. 2016. Structure-from-Motion Revisited. In *Conference on Computer Vision and Pattern Recognition (CVPR)*.
- Markus Schütz, Bernhard Kerbl, and Michael Wimmer. 2022. Software Rasterization of 2 Billion Points in Real Time. *Proc. ACM Comput. Graph. Interact. Tech.* 5, 3, Article 24 (Jul 2022), 17 pages. <https://doi.org/10.1145/3543863>
- Vincent Sitzmann, Justus Thies, Felix Heide, Matthias Nießner, Gordon Wetzstein, and Michael Zollhofer. 2019. Deepvoxels: Learning persistent 3d feature embeddings. In *Proceedings of the IEEE/CVF Conference on Computer Vision and Pattern Recognition*. 2437–2446.
- Noah Snavely, Steven M Seitz, and Richard Szeliski. 2006. Photo tourism: exploring photo collections in 3D. In *Proc. SIGGRAPH*.
- Carsten Stoll, Nilas Hasler, Juergen Gall, Hans-Peter Seidel, and Christian Theobalt. 2011. Fast articulated motion tracking using a sums of gaussians body model. In *2011 International Conference on Computer Vision*. IEEE, 951–958.
- Cheng Sun, Min Sun, and Hwann-Tzong Chen. 2022. Direct Voxel Grid Optimization: Super-fast Convergence for Radiance Fields Reconstruction. In *CVPR*.
- Towaki Takikawa, Alex Evans, Jonathan Tremblay, Thomas Müller, Morgan McGuire, Alec Jacobson, and Sanja Fidler. 2022. Variable bitrate neural fields. In *ACM SIGGRAPH 2022 Conference Proceedings*. 1–9.
- Towaki Takikawa, Joey Litani, Kangxue Yin, Karsten Kreis, Charles Loop, Derek Nowrouzezahrai, Alec Jacobson, Morgan McGuire, and Sanja Fidler. 2021. Neural Geometric Level of Detail: Real-time Rendering with Implicit 3D Shapes. (2021).
- Ayush Tewari, Justus Thies, Ben Mildenhall, Pratul Srinivasan, Edgar Tretschk, W Yifan, Christoph Lassner, Vincent Sitzmann, Ricardo Martin-Brualla, Stephen Lombardi, et al. 2022. Advances in neural rendering. In *Computer Graphics Forum*, Vol. 41. Wiley Online Library, 703–735.
- Justus Thies, Michael Zollhöfer, and Matthias Nießner. 2019. Deferred neural rendering: Image synthesis using neural textures. *ACM Transactions on Graphics (TOG)* 38, 4 (2019), 1–12.
- Angtian Wang, Peng Wang, Jian Sun, Adam Kortylewski, and Alan Yuille. 2023. VoGE: A Differentiable Volume Renderer using Gaussian Ellipsoids for Analysis-by-Synthesis. In *The Eleventh International Conference on Learning Representations*. https://openreview.net/forum?id=AdPjb9cud_Y

- Olivia Wiles, Georgia Gkioxari, Richard Szeliski, and Justin Johnson. 2020. Synsin: End-to-end view synthesis from a single image. In *Proceedings of the IEEE/CVF Conference on Computer Vision and Pattern Recognition*. 7467–7477.
- Xiuchao Wu, Jiamin Xu, Zihan Zhu, Hujun Bao, Qixing Huang, James Tompkin, and Weiwei Xu. 2022. Scalable Neural Indoor Scene Rendering. *ACM Transactions on Graphics (TOG)* (2022).
- Yiheng Xie, Towaki Takikawa, Shunsuke Saito, Or Litany, Shiqin Yan, Numair Khan, Federico Tombari, James Tompkin, Vincent Sitzmann, and Srinath Sridhar. 2022. Neural fields: visual computing and beyond. In *Computer Graphics Forum*, Vol. 41. Wiley Online Library, 641–676.
- Qiangeng Xu, Zexiang Xu, Julien Philip, Sai Bi, Zhixin Shu, Kalyan Sunkavalli, and Ulrich Neumann. 2022. Point-nerf: Point-based neural radiance fields. In *Proceedings of the IEEE/CVF Conference on Computer Vision and Pattern Recognition*. 5438–5448.
- Wang Yifan, Felice Serena, Shihao Wu, Cengiz Öztirol, and Olga Sorkine-Hornung. 2019. Differentiable surface splatting for point-based geometry processing. *ACM Transactions on Graphics (TOG)* 38, 6 (2019), 1–14.
- Alex Yu, Ruilong Li, Matthew Tancik, Hao Li, Ren Ng, and Angjoo Kanazawa. 2021. PlenOctrees for Real-time Rendering of Neural Radiance Fields. In *ICCV*.
- Qiang Zhang, Seung-Hwan Baek, Szymon Rusinkiewicz, and Felix Heide. 2022. Differentiable Point-Based Radiance Fields for Efficient View Synthesis. In *SIGGRAPH Asia 2022 Conference Papers* (Daegu, Republic of Korea) (SA ’22). Association for Computing Machinery, New York, NY, USA, Article 7, 12 pages. <https://doi.org/10.1145/3550469.3555413>
- Tinghui Zhou, Shubham Tulsiani, Weilun Sun, Jitendra Malik, and Alexei A Efros. 2016. View synthesis by appearance flow. In *European conference on computer vision*. Springer, 286–301.
- Matthias Zwicker, Hanspeter Pfister, Jeroen Van Baar, and Markus Gross. 2001a. EWA volume splatting. In *Proceedings Visualization, 2001. VIS’01*. IEEE, 29–538.
- Matthias Zwicker, Hanspeter Pfister, Jeroen van Baar, and Markus Gross. 2001b. Surface Splatting. In *Proceedings of the 28th Annual Conference on Computer Graphics and Interactive Techniques (SIGGRAPH ’01)*. Association for Computing Machinery, New York, NY, USA, 371–378. <https://doi.org/10.1145/383259.383300>

A DETAILS OF GRADIENT COMPUTATION

Recall that Σ/Σ' are the world/view space covariance matrices of the Gaussian, q is the rotation, and s the scaling, W is the viewing transformation and J the Jacobian of the affine approximation of the projective transformation. We can apply the chain rule to find the derivatives w.r.t. scaling and rotation:

$$\frac{d\Sigma'}{ds} = \frac{d\Sigma'}{d\Sigma} \frac{d\Sigma}{ds} \quad (8)$$

and

$$\frac{d\Sigma'}{dq} = \frac{d\Sigma'}{d\Sigma} \frac{d\Sigma}{dq} \quad (9)$$

Simplifying Eq. 5 using $U = JW$ and Σ' being the (symmetric) upper left 2×2 matrix of $U\Sigma U^T$, denoting matrix elements with subscripts, we can find the partial derivatives $\frac{\partial\Sigma'}{\partial\Sigma_{ij}} = \begin{pmatrix} U_{1,i}U_{1,j} & U_{1,i}U_{2,j} \\ U_{1,j}U_{2,i} & U_{2,i}U_{2,j} \end{pmatrix}$.

Next, we seek the derivatives $\frac{d\Sigma}{ds}$ and $\frac{d\Sigma}{dq}$. Since $\Sigma = RSS^T R^T$, we can compute $M = RS$ and rewrite $\Sigma = MM^T$. Thus, we can write $\frac{d\Sigma}{ds} = \frac{d\Sigma}{dM} \frac{dM}{ds}$ and $\frac{d\Sigma}{dq} = \frac{d\Sigma}{dM} \frac{dM}{dq}$. Since the covariance matrix Σ (and its gradient) is symmetric, the shared first part is compactly found by $\frac{d\Sigma}{dM} = 2M^T$. For scaling, we further have $\frac{\partial M_{i,j}}{\partial s_k} = \begin{cases} R_{i,k} & \text{if } j = k \\ 0 & \text{otherwise} \end{cases}$. To derive gradients for rotation, we recall the conversion from a unit quaternion q with real part q_r and imaginary parts q_i, q_j, q_k to a rotation matrix R :

$$R(q) = 2 \begin{pmatrix} \frac{1}{2} - (q_j^2 + q_k^2) & (q_i q_j - q_r q_k) & (q_i q_k + q_r q_j) \\ (q_i q_j + q_r q_k) & \frac{1}{2} - (q_i^2 + q_k^2) & (q_j q_k - q_r q_i) \\ (q_i q_k - q_r q_j) & (q_j q_k + q_r q_i) & \frac{1}{2} - (q_i^2 + q_j^2) \end{pmatrix} \quad (10)$$

As a result, we find the following gradients for the components of q :

$$\begin{aligned} \frac{\partial M}{\partial q_r} &= 2 \begin{pmatrix} 0 & -s_y q_k & s_z q_j \\ s_x q_k & 0 & -s_z q_i \\ -s_x q_j & s_y q_i & 0 \end{pmatrix}, & \frac{\partial M}{\partial q_i} &= 2 \begin{pmatrix} 0 & s_y q_j & s_z q_k \\ s_x q_j & -2s_y q_i & -s_z q_r \\ s_x q_k & s_y q_r & -2s_z q_i \end{pmatrix} \\ \frac{\partial M}{\partial q_j} &= 2 \begin{pmatrix} -2s_x q_j & s_y q_i & s_z q_r \\ s_x q_i & 0 & s_z q_k \\ -s_x q_r & s_y q_k & -2s_z q_j \end{pmatrix}, & \frac{\partial M}{\partial q_k} &= 2 \begin{pmatrix} -2s_x q_k & -s_y q_r & s_z q_i \\ s_x q_r & -2s_y q_k & s_z q_j \\ s_x q_i & s_y q_j & 0 \end{pmatrix} \end{aligned} \quad (11)$$

Deriving gradients for quaternion normalization is straightforward.

B OPTIMIZATION AND DENSIFICATION ALGORITHM

Our optimization and densification algorithms are summarized in Algorithm 1.

Algorithm 1 Optimization and Densification
 w, h : width and height of the training images

```

 $M \leftarrow$  SfM Points                                ▷ Positions
 $S, C, A \leftarrow$  InitAttributes()                  ▷ Covariances, Colors, Opacities
 $i \leftarrow 0$                                          ▷ Iteration Count
while not converged do
     $V, \hat{I} \leftarrow$  SampleTrainingView()           ▷ Camera V and Image
     $I \leftarrow$  Rasterize( $M, S, C, A, V$ )          ▷ Alg. 2
     $L \leftarrow$  Loss( $I, \hat{I}$ )                      ▷ Loss
     $M, S, C, A \leftarrow$  Adam( $\nabla L$ )            ▷ Backprop & Step
    if IsRefinementIteration( $i$ ) then
        for all Gaussians  $(\mu, \Sigma, c, \alpha)$  in  $(M, S, C, A)$  do
            if  $\alpha < \epsilon$  or IsTooLarge( $\mu, \Sigma$ ) then          ▷ Pruning
                RemoveGaussian()
            end if
            if  $\nabla_p L > \tau_p$  then                      ▷ Densification
                if  $\|S\| > \tau_S$  then                      ▷ Over-reconstruction
                    SplitGaussian( $\mu, \Sigma, c, \alpha$ )
                else                                     ▷ Under-reconstruction
                    CloneGaussian( $\mu, \Sigma, c, \alpha$ )
                end if
            end if
        end for
    end if
     $i \leftarrow i + 1$ 
end while

```

C DETAILS OF THE RASTERIZER

Sorting. Our design is based on the assumption of a high load of small splats, and we optimize for this by sorting splats once for each frame using radix sort at the beginning. We split the screen into 16x16 pixel tiles (or bins). We create a list of splats per tile by instantiating each splat in each 16×16 tile it overlaps. This results in a moderate increase in Gaussians to process which however is amortized by simpler control flow and high parallelism of optimized GPU Radix sort [Merrill and Grimshaw 2010]. We assign a key for each splats instance with up to 64 bits where the lower 32 bits encode its projected depth and the higher bits encode the index of the overlapped tile. The exact size of the index depends on how many tiles fit the current resolution. Depth ordering is thus directly resolved for all splats in parallel with a single radix sort. After

sorting, we can efficiently produce per-tile lists of Gaussians to process by identifying the start and end of ranges in the sorted array with the same tile ID. This is done in parallel, launching one thread per 64-bit array element to compare its higher 32 bits with its two neighbors. Compared to [Lassner and Zollhofer 2021], our rasterization thus completely eliminates sequential primitive processing steps and produces more compact per-tile lists to traverse during the forward pass. We show a high-level overview of the rasterization approach in Algorithm 2.

Algorithm 2 GPU software rasterization of 3D Gaussians

w, h : width and height of the image to rasterize
 M, S : Gaussian means and covariances in world space
 C, A : Gaussian colors and opacities
 V : view configuration of current camera

```

function RASTERIZE( $w, h, M, S, C, A, V$ )
    CullGaussian( $p, V$ )                                ▷ Frustum Culling
     $M', S' \leftarrow$  ScreenspaceGaussians( $M, S, V$ )      ▷ Transform
     $T \leftarrow$  CreateTiles( $w, h$ )
     $L, K \leftarrow$  DuplicateWithKeys( $M', T$ )            ▷ Indices and Keys
    SortByKeys( $K, L$ )                                  ▷ Globally Sort
     $R \leftarrow$  IdentifyTileRanges( $T, K$ )
     $I \leftarrow 0$                                          ▷ Init Canvas
    for all Tiles  $t$  in  $I$  do
        for all Pixels  $i$  in  $t$  do
             $r \leftarrow$  GetTileRange( $R, t$ )
             $I[i] \leftarrow$  BlendInOrder( $i, L, r, K, M', S', C, A$ )
        end for
    end for
    return  $I$ 
end function
```

Numerical stability. During the backward pass, we reconstruct the intermediate opacity values needed for gradient computation by repeatedly dividing the accumulated opacity from the forward pass by each Gaussian’s α . Implemented naively, this process is prone to numerical instabilities (e.g., division by 0). To address this, both in the forward and backward pass, we skip any blending updates with $\alpha < \epsilon$ (we choose ϵ as $\frac{1}{255}$) and also clamp α with 0.99 from above. Finally, **before** a Gaussian is included in the forward rasterization pass, we compute the accumulated opacity if we were to include it and stop front-to-back blending **before** it can exceed 0.9999.

D PER-SCENE ERROR METRICS

Tables 4–9 list the various collected error metrics for our evaluation over all considered techniques and real-world scenes. We list both the copied Mip-NeRF360 numbers and those of our runs used to generate the images in the paper; averages for these over the full Mip-NeRF360 dataset are PSNR 27.58, SSIM 0.790, and LPIPS 0.240.

Table 4. SSIM scores for Mip-NeRF360 scenes. \dagger copied from original paper.

	bicycle	flowers	garden	stump	treehill	room	counter	kitchen	bonsai
Plenoxels	0.496	0.431	0.6063	0.523	0.509	0.8417	0.759	0.648	0.814
INGP-Base	0.491	0.450	0.649	0.574	0.518	0.855	0.798	0.818	0.890
INGP-Big	0.512	0.486	0.701	0.594	0.542	0.871	0.817	0.858	0.906
Mip-NeRF360 \dagger	0.685	0.583	0.813	0.744	0.632	0.913	0.894	0.920	0.941
Mip-NeRF360	0.685	0.584	0.809	0.745	0.631	0.910	0.892	0.917	0.938
Ours-7k	0.675	0.525	0.836	0.728	0.598	0.884	0.873	0.900	0.910
Ours-30k	0.771	0.605	0.868	0.775	0.638	0.914	0.905	0.922	0.938

Table 5. PSNR scores for Mip-NeRF360 scenes. \dagger copied from original paper.

	bicycle	flowers	garden	stump	treehill	room	counter	kitchen	bonsai
Plenoxels	21.912	20.097	23.4947	20.661	22.248	27.594	23.624	23.420	24.669
INGP-Base	22.193	20.348	24.599	23.626	22.364	29.269	26.439	28.548	30.337
INGP-Big	22.171	20.652	25.069	23.466	22.373	29.690	26.691	29.479	30.685
Mip-NeRF360 \dagger	24.37	21.73	26.98	26.40	22.87	31.63	29.55	32.23	33.46
Mip-NeRF360	24.305	21.649	26.875	26.175	22.929	31.467	29.447	31.989	33.397
Ours-7k	23.604	20.515	26.245	25.709	22.085	28.139	26.705	28.546	28.850
Ours-30k	25.246	21.520	27.410	26.550	22.490	30.632	28.700	30.317	31.980

Table 6. LPIPS scores for Mip-NeRF360 scenes. \dagger copied from original paper.

	bicycle	flowers	garden	stump	treehill	room	counter	kitchen	bonsai
Plenoxels	0.506	0.521	0.3864	0.503	0.540	0.4186	0.441	0.447	0.398
INGP-Base	0.487	0.481	0.312	0.450	0.489	0.301	0.342	0.254	0.227
INGP-Big	0.446	0.441	0.257	0.421	0.450	0.261	0.306	0.195	0.205
Mip-NeRF360 \dagger	0.301	0.344	0.170	0.261	0.339	0.211	0.204	0.127	0.176
Mip-NeRF360	0.305	0.346	0.171	0.265	0.347	0.213	0.207	0.128	0.179
Ours-7k	0.318	0.417	0.153	0.287	0.404	0.272	0.254	0.161	0.244
Ours-30k	0.205	0.336	0.103	0.210	0.317	0.220	0.204	0.129	0.205

Table 7. SSIM scores for Tanks&Temples and Deep Blending scenes.

	Truck	Train	Dr Johnson	Playroom
Plenoxels	0.774	0.663	0.787	0.802
INGP-Base	0.779	0.666	0.839	0.754
INGP-Big	0.800	0.689	0.854	0.779
Mip-NeRF360	0.857	0.660	0.901	0.900
Ours-7k	0.840	0.694	0.853	0.896
Ours-30k	0.879	0.802	0.899	0.906

Table 8. PSNR scores for Tanks&Temples and Deep Blending scenes.

	Truck	Train	Dr Johnson	Playroom
Plenoxels	23.221	18.927	23.142	22.980
INGP-Base	23.260	20.170	27.750	19.483
INGP-Big	23.383	20.456	28.257	21.665
Mip-NeRF360	24.912	19.523	29.140	29.657
Ours-7k	23.506	18.892	26.306	29.245
Ours-30k	25.187	21.097	28.766	30.044

Table 9. LPIPS scores for Tanks&Temples and Deep Blending scenes.

	Truck	Train	Dr Johnson	Playroom
Plenoxels	0.335	0.422	0.521	0.499
INGP-Base	0.274	0.386	0.381	0.465
INGP-Big	0.249	0.360	0.352	0.428
Mip-NeRF360	0.159	0.354	0.237	0.252
Ours-7k	0.209	0.350	0.343	0.291
Ours-30k	0.148	0.218	0.244	0.241